ACS APPLIED MATERIALS & INTERFACES

Research Article

www.acsami.org

Stoichiometry Gradient, Cation Interdiffusion, and Band Alignment between a Nanosized TiO_2 Blocking Layer and a Transparent Conductive Oxide in Dye-Sensitized Solar Cell Front Contacts

Gabriele Salvinelli,[†] Giovanni Drera,[†] Camilla Baratto,[‡,§] Antonio Braga,[§] and Luigi Sangaletti*[,†]

[†]Interdisciplinary Laboratories for Advanced Materials Physics (I-LAMP) and Dipartimento di Matematica e Fisica, Università Cattolica del Sacro Cuore, I-25121 Brescia, Italy

[‡]CNR INO Sensor Lab, Via Branze 45, 25133 Brescia, Italy

[§]University of Brescia, Dept. of Information Engineering, Via Valotti 9, 25133 Brescia, Italy

ABSTRACT: An angle−resolved photoemission spectroscopy study allowed us to identify cation interdiffusion and stoichiometry gradients at the interface between a nanosized TiO_2 blocking layer and a transparent conductive Cd−Sn oxide substrate. A stoichiometry gradient for the Sn cations is already found in the bare Cd−Sn oxide layer. When TiO_2 ultrathin layers are deposited by RF sputtering on the Cd−Sn oxide layer, Ti is found to partially replace Sn, resulting in a Cd−Sn−Ti mixed oxide layer with a thickness ranging from 0.85 to 3.3 nm. The band gap profile across the junction has been reconstructed for three TiO_2 layers, resulting in a valence band offset decrease (and a conduction band offset increase) with the blocking layer thickness. The results are related to the cell efficiencies in terms of charge injection and recombination processes.

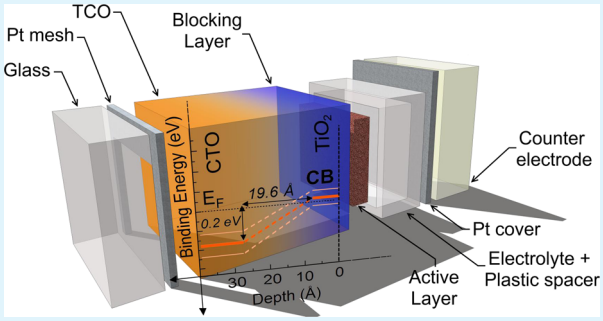

KEYWORDS: *photoemission, solar cell, DSSC, front contact, blocking layer, band alignment*

Ultrathin interfaces are playing a key role in the development of new architectures to be tested in photovoltaic (PV) applications.[1,2] Novel devices can be engineered provided that the capability to control interfaces at the nanoscale is demonstrated. Among the most popular solar cells, electrochemical PV cells display a stack of interfaces with different thickness and chemical properties, from the front contact to the back electrode.[3] The front contact constitutes itself an interface where a transparent conducting oxide (TCO) layer is usually matched with a nanosized blocking layer (BL). The quality of this interface may have relevant consequences on the overall cell performances.[4−7]

At one side of the front contact interface a TCO thin layer is found, which exhibits high optical transmittance and high electrical conductivity at the same time. This combination of properties is usually impossible to achieve in intrinsic or undoped oxides; therefore, it is obtained by way of non-stoichiometric compositions or through doping the pristine materials with appropriate elements. Bädeker was the first to discover the TCO qualities in 1907 by the thermal oxidation of sputtered Cd thin films.[8] Since then, TCOs have been pervasively studied because of their wide variety of technology applications, such as flat panel displays, photovoltaic (PV) cells, optoelectronic devices, transparent thin films transistors, gas sensors, low-emissivity windows, and thin-film resistors.[9]

Most of the commercially available TCOs are binary or ternary compounds containing one or two metallic elements. Although a single phase is essential to reach high electrical conductivity together with low optical absorbance,[10] the crystal phase of thin films is not strictly required for TCOs. For example, Nozik[11] prepared amorphous Cd_2SnO_4 thin films with a wide range of conductivities, retaining high visible transmittance, in which oxygen vacancies provided the donor states. Hosono et al.[12] deposited wide-gap Cd-based amorphous oxides, relating the high electron conductivity either to the formation of oxygen vacancies or to ion implantation of excess cations. Recently, in the frame of PV application, a non-stoichiometric amorphous cadmium−tin oxide $Cd_xSn_yO_z$ (CTO) thin film, prepared by RF sputtering, was matched with ultrathin TiO_2 BL, representing a reliable solution for dye-sensitized solar cells (DSSCs) manufacturing.[13]

On the other side of the front contact interface a BL is found, which in the common scheme of DSSCs prevents the recombination of the injected electrons into the front contact with the oxidized species in the electrolyte,[14−16] leading to an increase either in the photocurrent density[17,18] or the open-circuit voltage[19] or both.[14,20−22] Several studies account for the advantages due to the BL presence at the photoanodes, but its role is still debated because the resulting effects can be different on a case-by-case basis. Besides, the chemical composition, the

Received: October 17, 2014
Accepted: December 3, 2014
Published: December 3, 2014

   dx.doi.org/10.1021/am5072018 | *ACS Appl. Mater. Interfaces* 2015, 7, 765−773

Table 1. DSSC efficiency (η), Efficiency Improvements, Short Circuit Current (J_{SC}), Open Circuit Voltage (V_{OC}), and Fill Factor (FF) (Taken from Ref 7)[a]

sample	η (%)	improv.	J_{SC} (mA cm^{-2})	V_{OC} (V)	FF (#)	XPS Sn 3d/Cd 3d	abrupt model Sn 3d/Cd 3d	intermix model Sn 3d/Cd 3d
CTO	2.28 ± 0.05		4.45	0.76	0.67	1.92 ± 0.08	1.92	
CTO-TO15	2.87 ± 0.05	+25%	5.12	0.75	0.74	1.69 ± 0.01	1.91 ± 0.27	1.60 ± 0.10
CTO-TO30	3.12 ± 0.05	+36%	5.32	0.78	0.75	1.01 ± 0.03	1.84 ± 0.20	1.04 ± 0.05
CTO-TO60	3.05 ± 0.05	+33%	5.12	0.76	0.77	0.45 ± 0.10	1.75 ± 0.19	0.44 ± 0.02

[a]Quantification analysis of the Sn/Cd ratio from experimental XPS spectra, calculated XPS spectra within the abrupt model and the intermix model. Experimental and calculated XPS spectra are displayed in Figure 1a.

crystal phase, the thickness, and even the deposition method, for the most efficient BL, are not univocally defined yet.

In this paper, the heterojunction between a CTO layer and an ultrathin TiO_2 (TO) BL is studied by angle-resolved X-ray photoelectron spectroscopy (AR-XPS). These layers constitute the front contact of the DSSCs prepared in ref 7. As the TO thickness is known to affect the overall efficiency of the solar cell,[7,17,20,23,24] in the present study, different BL thicknesses have been considered, with the aim to relate the physical properties of the interface with the cell performances.

In particular, (i) the chemical composition, (ii) the stoichiometry gradient, and (iii) the cation interdiffusion, which occurs at the CTO/TO heterojunction, have been tracked, providing a nondestructive effective depth profiling across the interface. Finally, on the basis of the band offset method developed by Kraut et al.[25,26] the band diagram was reconstructed for each heterointerface relating the DSSC efficiency improvements to the BL thickness and barrier height.

MATERIALS AND METHODS

TiO_2–$CdSn_xO_y$ Heterostructure Fabrication. The CTO-TO interfaces under investigation were obtained by radio frequency (RF) sputtering as described in ref 7, where the deposition process and the functional properties of the DSSCs are fully detailed. The area of the tested prototypes ranged from 4 × 4 mm^2 to 5 × 6 mm^2. A 650 nm thick CTO film was grown onto a clean Si (100) wafer. The substrate was kept at 400 °C in an inert (Ar) atmosphere for 2 h at the constant pressure of 5 × 10^{-3} mbar for the CTO, while an oxidizing atmosphere (Ar/O_2 equal to 90–10%) was used for the TiO_2 growth with three different deposition times (15 min for CTO-TO15, 30 min for CTO-TO30, and 1 h for CTO-TO60). The main functional features of the DSSCs are reported in ref 7. and the cell efficiency values are recalled in Table 1. The multilayers prepared on Si wafer for the XPS analysis and those deposited on glass for the application in DSSCs were grown at the same time.

Experimental Setup. The XPS data were collected with the Mg Kα-line ($h\nu$ = 1253.6 eV) of a dual-anode PsP X-ray source, running at a power of about 110 W. Photoelectrons were collected using a SCIENTA R3000 analyzer, operating in an ultrahigh vacuum chamber with a base pressure of 2 × 10^{-10} mbar. The analyzer was properly calibrated according to the procedure described in ref 27.

Calculation of Electron Signal Attenuation. The interface modeling from the XPS peak angular dependence was carried out with the BriXias code (see ref 27 for further details), based on the IGOR Pro 6.3 programming language. It includes a computational engine, based on standard databases and state-of-the-art Monte Carlo code, designed to predict XPS spectra on complex multilayer structure, carefully considering the experimental geometry and the features of the X-ray source. The XPS core-level peak area of a selected layer at a depth d with a thickness t can be evaluated through the following formula:

$$I(E_k, \theta) = K \int_d^{d+t} \Phi(E_k, \theta, z)\mathrm{d}z$$

where K is a normalization constant, which includes the photoionization cross section,[28] the atomic density of the species, and analyzer-dependent parameters; $\Phi(E_k, \theta, z)$ is the generic escape probability (known as the depth distribution function, DDF) of an electron generated at a depth z with a kinetic energy E_k at an angle θ with respect to the surface normal. According to the Lambert–Beer law, the DDF function is usually approximated by a Poisson distribution[29] $\Phi = \exp[-z/(\lambda \times \cos\theta)]$, where λ is the inelastic mean free path (IMFP) of the photoelectrons.[30] Such an approximation leads to a simple analytical expression for the peak areas, which is defined as *straight line motion* by Tilinin et al.[31] However, this formulation may result in an overestimation of the top layer thickness, especially for thin overlayers.

Here, we exploit Monte Carlo (MC) DDF calculations based on the algorithm described by Werner,[29] in order to include both inelastic and elastic electronic scattering processes in the so-called transport approximation (TA).[32] Furthermore, the photoemission asymmetry parameters are taken into account for each core level and MC calculations of electronic trajectories are computed to predict the XPS peak areas in CTO-TO interface, since an analytic DDF formulation[31] cannot be written for a generic multilayer sample.

RESULTS AND DISCUSSION

XPS Results. To evaluate the Cd and Sn stoichiometry in the bulk CTO, normal emission XPS data were collected for each heterostructure in the 400–500 eV binding energy region, where the Cd 3d, Ti 2p, and Sn 3d core levels are detectable, as displayed in Figure 1a. The spectra were properly normalized with respect to the analyzer transmission. The core level satellites of the nonmonochromatized X-ray source were removed by a deconvolution procedure and an universal-cross section Tougaard background[33] was subtracted from the experimental data. The resulting Sn/Cd stoichiometry ratio values are listed in Table 1. As can be observed, the Sn/Cd stoichiometry ratio values decrease with the thickness, ranging from 1.92 ± 0.08 for the bare CTO layer to down to 0.45 ± 0.10 for the CTO-TO60 interface. The stoichiometry variation of the Sn 3d/Cd 3d ratio as a function of the TO deposition time could be explained by referring to two mechanisms: a stoichiometry gradient in the CTO surface and/or a substitution of different cation species across the interface. Both effects can be studied by means of an AR-XPS analysis. The investigation of these mechanisms constitutes the goal of the next subsections.

CTO AR-XPS Results. To investigate the Sn/Cd stoichiometry, an AR-XPS analysis was carried out for the bare CTO, as shown in Figure 2. The integrated Cd 3d and Sn 3d core level areas were collected in the 0–80° polar angle (θ) range (see the inset of Figure 1b) with steps of 4°. All data were normalized by setting the Cd 3d intensity values equal to 1. Data in Figure 2 clearly evidence a pronounced variation of the Sn/Cd ratio with the polar angle in the bare CTO. This indicates the presence of a stoichiometry gradient of the metal cations for the bare CTO close to the surface, that is, at high θ

dx.doi.org/10.1021/am5072018 | ACS Appl. Mater. Interfaces 2015, 7, 765–773

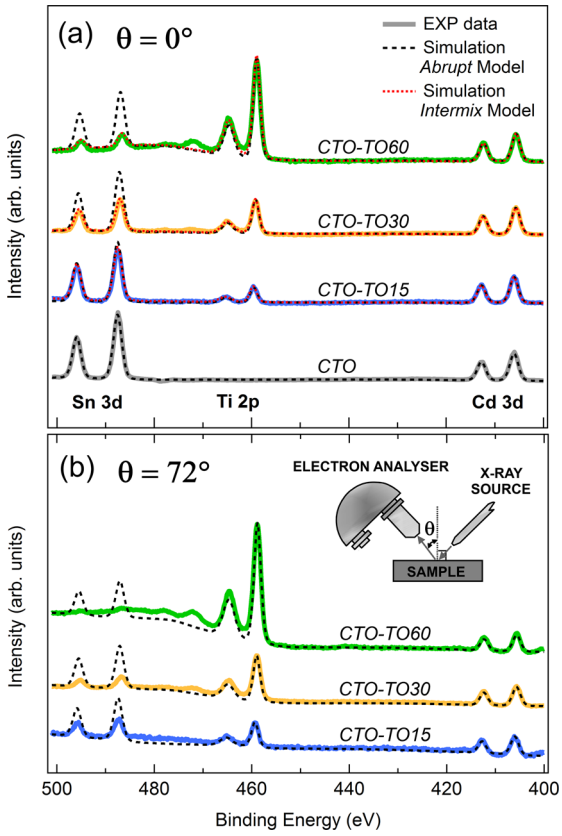

Figure 1. Experimental XPS data (solid lines) for the bare CTO and CTO-TOs collected at the polar angle $\theta = 0°$ (a) and at $\theta = 72°$ (b). Calculated XPS spectra within the abrupt interface model (black-dashed) and the intermix model (red-dotted). All the spectra are normalized to the Cd 3d peak area. Inset: Experimental setup geometry, with the polar angle θ.

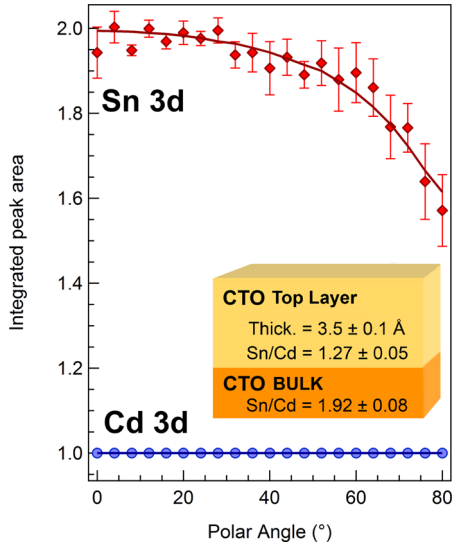

Figure 2. AR-XPS data on the Cd 3d (blue dots) and Sn 3d (red diamonds) core levels for bare CTO. Fitting curves are displayed as solid lines. The integrated peak areas are normalized with respect to the Cd 3d values. Inset: effective two-layer model resulting from the fitting procedure of the AR-XPS.

values, where the surface sensitivity of the XPS probe is known to be enhanced.

In the modeling carried out by using the BriXias code,[27] the fitting algorithm is tuned to reproduce the experimental data (i.e., the peak intensity dependence on the polar angle θ) using as fitting parameters the thickness of each layer above the bulk material.

The AR-XPS data fitting shown in Figure 2 is based on the model described in the inset of Figure 2, which is able to reproduce the same Sn/Cd stoichiometry gradient. This model consists of two effective layers: the CTO bulk layer, which is characterized by a Sn/Cd ratio equal to 1.92 as measured by XPS in normal emission (see Table 1), and the CTO top layer, which shows a reduced Sn/Cd stoichiometry equal to 1.27 for an estimated thickness of 3.5 ± 0.1 Å. These values of stoichiometry and top layer thickness are those yielding the best fit of the experimental AR-XPS data (points in Figure 2) with the model calculations (continuous lines in Figure 2).

The Abrupt Model for XPS and AR-XPS in CTO-TOs. Figure 3 shows the AR-XPS data collected from the CTO-TOs heterojunctions in the 0−52° polar angle range. Here, in addition to the Cd and Sn AR-XPS intensity profile, the Ti 2p intensity profile is shown. To interpret the experimental data, we considered a simple model (hereafter called abrupt model, displayed in Figure 4a) based on an abrupt interface between a continuous film of TiO_2 (the BL) and the effective two-layer model of Figure 2, developed for the CTO.

For the present model, the convergence of the fitting procedure is achieved only for the CTO-TO15 sample (Figure 3a), whereas a large mismatch occurs for the other samples (Figure 3b and c) up to the inversion of the Cd 3d and Sn 3d fitting curves in the CTO-TO60 (Figure 3c). On the other hand, the fit appears to reproduce the angular (i.e polar angle) dependence of the data, as is evident when the fitting curves are vertically shifted by suitable offset values.

Therefore, the abrupt model well fits the bare CTO behavior but is inappropriate to model the CTO-TOs heterojunctions because of a clear stoichiometry mismatch (offset) between theory and experiment. These limits can also be retrieved from Figure 1a, which shows the comparison between the experimental data (solid lines) with the calculated XPS spectra (black-dashed lines). With the exception of the bare CTO, the model overestimates the Sn 4d core line peak intensity, thereby affecting the Sn/Cd ratios as summarized in Table 1.

The Intermix Model for XPS and AR-XPS in CTO-TOs. In order to improve the interface modeling, an extra process—that is, the interdiffusion of metal cations—was considered. Interdiffusion was properly accounted for by a model (hereafter denoted as the intermix model) where the substitution between different metal cation species can occur at the interface of each CTO-TO heterojunction, while the Sn/Cd stoichiometry gradient presented in the CTO AR-XPS Results section is maintained in the bulk material. The cations involved in the interdiffusion process appear to be Ti and Sn; this is consistent with the results of Figure 1b, which shows the comparison between data collected at a $\theta = 72°$ polar angle for the CTO-TOs and the XPS spectra calculated on the basis of the abrupt model. At such a grazing electron takeoff angle both Sn and Cd peak intensities result to be attenuated, as the bulk contribution is reduced in this geometry. However, the Sn 3d attenuation is larger than that measured for Cd 3d indicating that Sn could be replaced by Ti during the growth of the BL at the topmost layers of CTO. Moreover, the Sn 3d signal tends to disappear in the experimental spectrum of CTO-TO60 (green-solid line)—in contrast with the XPS simulations (black-dashed

dx.doi.org/10.1021/am5072018 | ACS Appl. Mater. Interfaces 2015, 7, 765−773

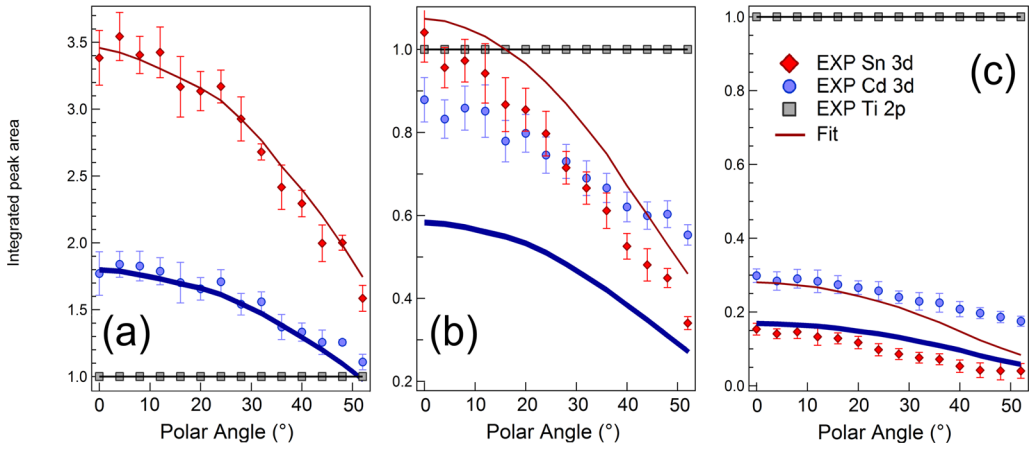

Figure 3. AR-XPS data for (a) CTO-TO15, (b) CTO-TO30, and (c) CTO-TO60. The integrated peak areas for the Cd 3d (blue dots), Sn 3d (red diamonds), and Ti 2p (gray squares) are collected from 0° to 52° of the polar angle θ. All data are normalized setting the Ti 2p values equal to 1. The fitting curves (solid lines) are obtained on the basis of the abrupt interface model (Figure 4a); Cd 3d thick blue line, Sn 3d thin-red line.

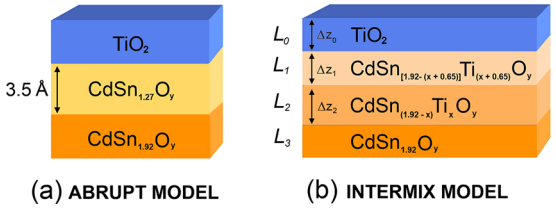

Figure 4. (a) Abrupt model: TiO_2 continuous film and the two-layer model for the CTO (Figure 2), which accounts for only the Sn/Cd stoichiometry gradient. (b) Effective four-layer intermix model. From the left: labels for each layer L_i (i = 0,1,2,3), labels for each thickness Δz_i, and the chemical formulas for the Ti ↔ Sn interdiffusion process.

line)—while the Cd 3d peak is still well detectable, showing the present limits of the abrupt model.

The basic idea of the intermix model is that Sn in the bare CTO can be substituted by Ti during the RF-magnetron sputtering deposition, thus changing the bulk composition, while maintaining the stoichiometry gradient very close to the original value at the same time. Modeling is achieved by adding two effective layers (hereafter denoted as L_1 and L_2) sandwiched between the TO (L_0) and CTO (L_3) layers, as shown in Figure 4b. Starting from the surface, the following layers appear: a continuous film of TiO_2 (L_0), two layers aimed to account for the cation interdiffusion and the stoichiometry

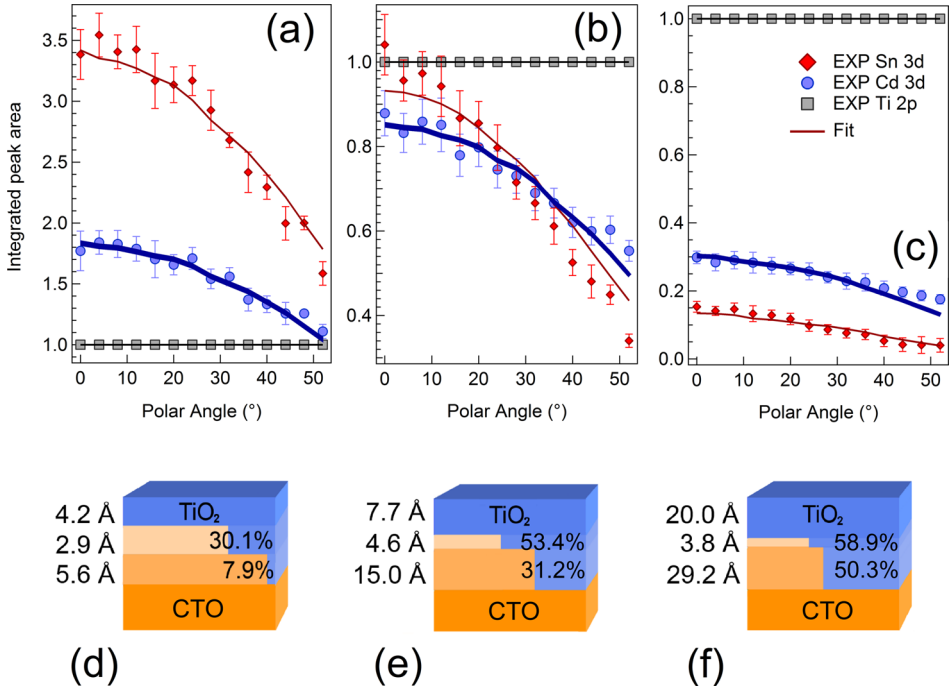

Figure 5. AR-XPS data for (a) CTO-TO15, (b) CTO-TO30, and (c) CTO-TO60. The integrated peak areas for the Cd 3d (blue dots), Sn 3d (red diamonds), and Ti 2p (gray squares) are collected in the 0° to 52° range of the polar angle θ. Fitting curves within the intermix model are displayed as solid lines; thick-blue line for Cd 3d and thin-red line for Sn 3d. All data are normalized by setting the Ti 2p intensity values equal to 1. The four-layer model resulting from the fitting procedure are displayed in (d) for CTO-TO15, (e) for CTO-TO30, and (f) for CTO-TO60; on the left the resulting thicknesses are shown, while inside each layer the Ti percent occupancy is reported. The complete set of the resulting parameters from the fitting analysis is listed in Table 2.

dx.doi.org/10.1021/am5072018 | ACS Appl. Mater. Interfaces 2015, 7, 765−773

gradient (L_1 and L_2) and a bulk layer for CTO (L_3). Considering the XPS stoichiometry evaluations of Table 1, L_3 presents a fixed Sn/Cd ratio of 1.92 for all the samples, while L_2 and L_1 are arranged in order to allow for Sn substitution with Ti as

$$Cd\,Sn_{(1.92-x)}Ti_xO_y \quad (1)$$

at the L_2 layer, and

$$Cd\,Sn_{[1.92-(x+\alpha)]}Ti_{(x+\alpha)}O_y \quad (2)$$

at the L_1 layer, where 1.92 is the Sn bulk stoichiometry in CTO and x equals the difference between 1.92 and the Sn/Cd experimental value for each CTO-TO (see Table 1). Finally, α is an effective value accounting for further Sn replacement with Ti in the L_1 layer (which is the closest to the growing TO layer during the deposition process). The α value is regarded as a fitting parameter and, for the present experiment, α resulted to be 0.65 ± 0.05.

Figure 5a–c shows the fitting results obtained with the intermix model for CTO-TOs, having set the thickness of each layer (Δz_i, i = 0,1,2) as a fitting parameter. The results are summarized in Table 2, while the corresponding four-layers

Table 2. Fitting Results for the AR-XPS Data of Figure5 by Using the Intermix Model of Figure 4b[a]

intermix model	CTO-TO15 (Å)	CTO-TO30 (Å)	CTO-TO60 (Å)
Δz_0	4.2	7.7	20.0
Δz_1	2.9	4.6	3.8
Δz_2	5.6	15.0	29.2
avg. Δz_{BL}	5.5–12.7	16.0–27.3	37.4–53.0
expt. Δz_{XRR} [*]	10.9	21.9	46.7

[a] Δz_{0-2} are the thicknesses for the effective layers L_{0-2}, Δz_{BL} is the average thickness for the BL while Δz_{XRR} is the experimental measurement of the BL thickness by XRR. Δz_{0-2} are defined within ±0.1 Å of uncertainty. [*] from ref 7.

effective models are depicted in Figure 5d–f. The average thickness Δz_{BL} for the TO film has been estimated by setting as upper limit the bare sum of Δz_i and as lower limit the sum of Δz_i with each term weighted by the estimated Ti concentration. Incidentally, it is important to remark that the present Δz_{BL} values are consistent with those (expt. Δz_{XRR} in Table 2) independently obtained from X-ray reflectivity (XRR).[7]

The reliability of the AR-XPS analysis can also be evaluated by the comparison between the experimental (solid lines) and the XPS spectra calculated by the intermix model (red-dotted lines), as presented in Figure 1a. Now, the peak intensities of the calculated spectra well reproduce the experimental data (see Table 1).

Interface Band Diagram. The interface band diagram of the present heterojunctions can be drawn by considering the layer thickness study so far carried out and the evaluation of the energy offsets of the interface layers with respect to the parent (CTO and TO) compounds. In order to retrieve the required energy values, an analysis of the valence band (VB) and the conduction band (CB) offset was carried out referring to a recent work of Goldfarb et al.[34] Indeed, by means of the binding energy (BE) of the Ti 3p and Cd 4d shallow core levels, as well as the VB maximum (VBM), the effective band diagram at the interfaces can be reconstructed.

Figure 6a shows the XPS spectra taken into account, that is, the two bulk references—the CTO and a 50 nm thick TiO_2/

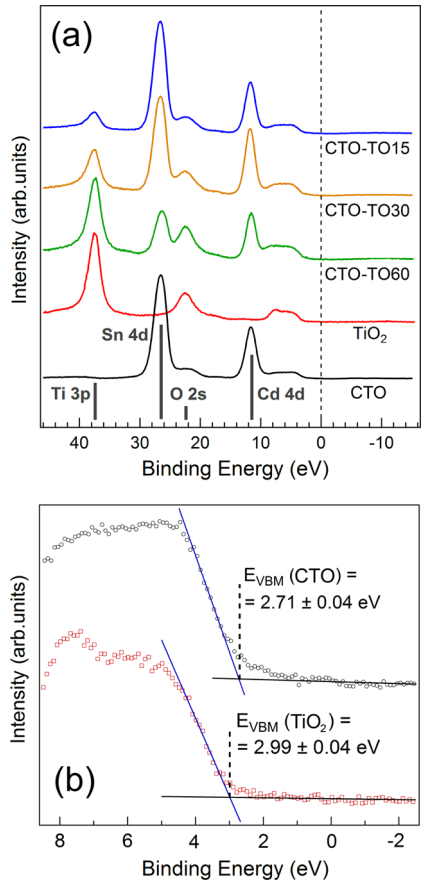

Figure 6. (a) Extended XPS data in the Ti 3p, Sn 4d, Cd 4d, and VB binding energy range for the CTO-TOs heterostructures and the parent compounds (CTO and TiO_2). The core level position are marked by gray bars, which are proportional to the photoemission cross sections. (b) Enlargement of the VB of CTO (black circles) and TiO_2 (red squares) and extrapolation of the VBM. E_{VBM} values for CTO and TiO_2 are reported in the panel.

Si(100)—and the three CTO-TOs heterostructures. Since the samples were in ohmic contact with a gold clip during the XPS measurements, all spectra are aligned in BE considering the energy of Au $4f_{7/2}$ equal to 83.98 eV.[35,36] The BEs for the Cd 4d and Ti 3p core levels are indicated in Figure 7b and c. The VBM is determined by extrapolating the leading edge of the VB spectra to the energy axis in order to account for the instrumental broadening. This procedure is displayed in Figure 6b and the VBM values for CTO and TiO_2 are shown in the same graph. The reliability of the VBM evaluation has been verified by considering the study of Chambers et al.[37] The VB offsets in CTO-TOs are determined as follows:

$$\Delta E_V(\text{CTO-TOs}) = \Delta E_{CL-VBM}(TiO_2) - [\Delta E_{CL-VBM}(\text{CTO}) + \Delta E_{CL}(\text{CTO-TOs})] \quad \text{(eq 3)}$$

where $\Delta E_{CL\text{-}VBM}$ is the difference between the BE of the shallow core level (Ti 3p or Cd 4d, in the present case) and the VBM in the selected bulk material (respectively, TiO_2 or CTO) while ΔE_{CL} is the difference between the BE of the selected shallow core levels in the heterostructures. Thereafter, the CB offset is estimated from ΔE_V by

dx.doi.org/10.1021/am5072018 | ACS Appl. Mater. Interfaces 2015, 7, 765–773

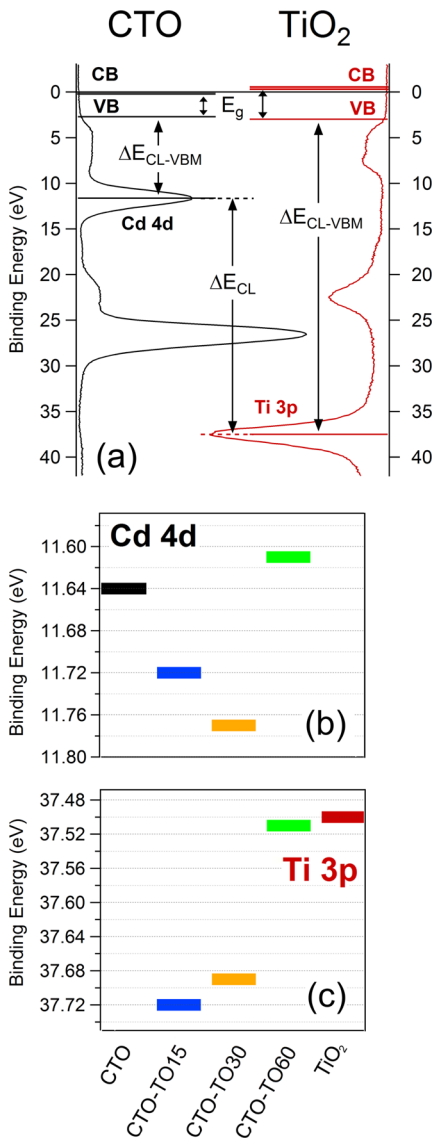

Figure 7. (a) Scheme of the energy levels considered for the band offset analysis. XPS spectra for CTO (left) and TiO_2 (right) are displayed on the panel sides. BE positions of the Cd 4d and Ti 3p core levels for the heterostructures CTO-TOs and the parent compounds are reported in panels b and c, respectively. The line thickness accounts for the uncertainty of the BE position, which is less than ±0.01 eV.

$$\Delta E_C(\text{CTO-TOs}) = [E_g(TiO_2) + \Delta E_V(\text{CTO-TOs})] - E_g(\text{CTO}) \quad (4)$$

where E_g is the energy gap, which is within the range 2.7−3.1 eV for CTOs.[38] Since the bare CTO is conductive,[7,13,39] we consider that the energy gap is less than the VBM = 2.71 eV, such that the CB is just below the Fermi level. States at the Fermi edge (E_F) are not clearly detected with the present XPS probe, likely due to the low XPS cross-section for oxygen, which is supposed to mainly contribute to filled states in the VB region.[40] However, the CTO VB spectrum shows a tail of states on the low BE side that may eventually yield a nonzero spectral weight at E_F. Referring to *T.* Meng et al.[41] that have systematically studied the E_g dependence on the Sn/Cd ratio, we have selected $E_g(\text{CTO}) = 2.66 \pm 0.05$ eV. On the other hand, for TiO_2 we assume the energy gap of the anatase phase, that is, 3.20 eV,[42] which is proved to be predominant in the film as reported in ref 13 by glancing incident X-ray diffraction (GIXRD) measurements on samples grown in similar conditions.

The scheme of the energy levels is shown in Figure 7a while the resulting ΔE_V and ΔE_C are listed in Table 3. Here, the band offset results are referred to the bulk CTO and TiO_2, represented by L_3 and L_0 respectively. The VBM shift in the L_1 and L_2 regions cannot be directly accessed by the present method, and therefore, the energy levels of the end members (CTO and TO) have been connected by straight lines as a guide for the eye.

Table 3. Valence Band Offsets (ΔE_V), Conduction Band Offsets (ΔE_C), and the Insulating Barrier (IB) Considering the Selected Bang Gap of E_g(CTO) = 2.66 eV and $E_g(TiO_2)$ = 3.20 eV[a]

sample	ΔE_V (eV)	ΔE_C (eV)	IB (eV)
CTO-TO15	−0.42	0.12	−0.01 ± 0.04
CTO-TO30	−0.34	0.20	0.02 ± 0.04
CTO-TO60	−0.32	0.22	0.20 ± 0.04

[a]The minus sign in the offsets means that the band maximum value of the bulk material in the heterojunction presents a BE lower than the one related to the film. ΔE values are defined within ±0.1 eV of uncertainty. All these values are displayed in Figure 8.

The following results are obtained for all the CTO-TOs: (i) the heterojunction is of type I (straddling gap) as shown in Figure 8d−f; (ii) the type I character is maintained independently on the BL thickness, and (iii) ΔE_C increases with the BL thickness as reported in Table 3. Furthermore, from the details of the CB region displayed in Figure 8a−c, it turns out that (iv) the insulating barrier (IB), which exceeds the Fermi energy and is generated by the BL in the L_0 layer, increases with the BL thickness. Therefore, we can establish that (v) the increase of the IB size can make the heterojunction more efficient for an application in a DSSC—at least in terms of minimizing the electron recombination—in view of the correlation of the efficiency gain with the increase of the BL average thickness. This is indeed demonstrated by comparing the IB size (Table3) and the DSSC efficiency (Table 1): in the CTO-TO15 the lowest efficiency is combined with an IB < 0 eV while in CTO-TO30 the best efficiency occurs when IB > 0 eV.

On this basis, the DSSC efficiency is expected to increase with the BL thickness, and thereby, the CTO-TO60 should exhibit the highest efficiency. This actually does not occur and similar behaviors can be found in several studies.[17,18,43−45,47,48] In order to rationalize the efficiency reduction beyond a critical thickness of the BL, both the IB and the ΔE_C have to be taken into account. In fact, CTO-TO30 and CTO-TO60 show a similar ΔE_C in contrast with a different IB. This situation is ascribed to the upward shift of the whole band across the junction which makes the CB of CTO-T60 closer to E_F in the L_3 layer (CTO) and well above E_F in the L_0 layer (TO). In this way, the IB of CTO-T60 results to be higher in energy and larger in depth. This may yield a reduction of the injection rate, justifying the efficiency reduction, which is usually found when the BL is *too* thick.

In conclusion, the blocking layer (BL) generates an insulating barrier between the nanocrystalline TiO_2 layer and

dx.doi.org/10.1021/am5072018 | ACS Appl. Mater. Interfaces 2015, 7, 765−773

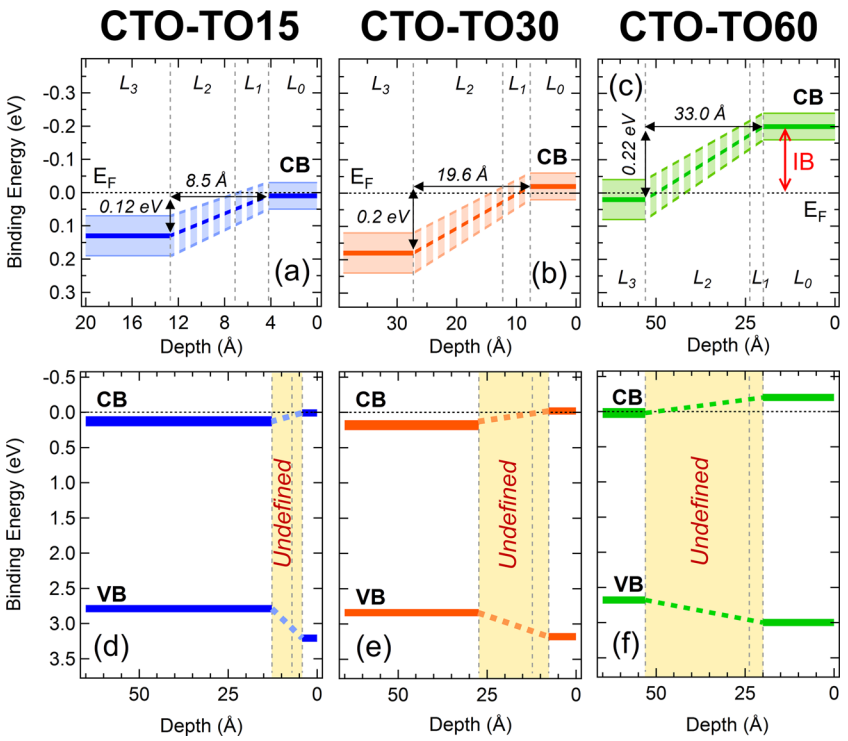

Figure 8. Effective band diagram for the VB and the CB of the heterostructures based on the intermix model results for CTO-TO15 (d), CTO-TO30 (e), and CTO-TO60 (f). (a, b, and c) Enlargements for CB. The insulating barrier (IB) is evidenced by the red arrow. The shadow region in panels a, b, and c and the thickness of the lines in panels d, e, and f stand for the uncertainty equal to ±0.04 eV except for the CTO CB, which is ±0.06 eV.

the TCO, which is found to improve the overall efficiency in the present DSSCs as long as its size is smaller than the critical value from about 2.2 to 4.7 nm (Δz_{BL} for CTO-TO30 and CTO-TO60, Table 2). In this case, the injection rate should prevail over the electron recombination rate. Otherwise, in agreement with refs 17 and 47, the evident upward band shift in CTO-TO60 with respect to CTO-TO30 could be an hint to state that the IB can almost inhibit the recombination process but at the expense of an injection rate reduction for a BL thickness larger than the critical value, negatively affecting the cell efficiency. Therefore, the best performances of the CTO-TO30 cell can be ascribed to a subtle balance between the barrier thickness (large enough to prevent electron recombination, that is, tunneling from CTO back to the electrolyte) and the increased CB energy offset (0.2 eV) with respect to the CTO-TO15 case (0.12 eV). On the other hand the CTO-TO60 junction displays the largest offset (0.22 eV), which is favorable to avoid electron recombination, but its BL thickness could be too large to enable an efficient charge (electron) transport from the TiO_2 nanocrystals to CTO.

DISCUSSION

Several works have so far presented a study of the DSSC efficiency in relation with the BL thickness, but only some of these have shown an efficiency reduction above a critical thickness of the BL. Other factors affecting the DSSC performance have also been proposed, such as a reduction of the light transmittance due to the BL thickness[43] or an increment of the internal series resistance of the solar cell.[44,45]

In Table 4 we have listed the studies where the BLs are based on TiO_2 and prepared by different deposition techniques, such as RF-magnetron sputtering, DC-magnetron sputtering, spray pyrolysis, atomic layer deposition (ALD), spin-casting, and electrodeposition.

Table 4. Comparison among Devices where the Front Contact Is the Heterojunction between a TCO and a TiO_2 BL Deposited by Different Techniques[a]

deposition technique	RPE (%)	TBE (nm)	ref.
RF-magnetron sputtering	+36	2.2	CTO-TO30
	+21	16	17
	+26	93	19
DC-magnetron sputtering	+10	18	44
	+42	300	45
spray pyrolysis	+11	75	46
	+87	150	47
ALD	+29	25	48
electrodeposition	+59	450	43
spin-casting	+33	160	22

[a]From the left: relative percent enhancement (RPE) for DSSC efficiency between a bare TCO front contact and the TCO/BL front contact, which exhibits the best cell efficiency and the BL thickness for the best efficiency (TBE).

In particular, we have focused on two parameters to be compared with our results: (i) the relative percent enhancement (RPE) of the DSSC efficiency between the cell with the front contact formed by the bare TCO (without BL) and the cell with the TCO/BL heterojunction as front contact which exhibits the highest efficiency and (ii) the BL thickness yielding the best efficiency (TBE). We note that CTO-TO30 shows the highest RPE for the RF-magnetron sputtering technique (+36%) and the overall best ratio between RPE and TBE. In fact, CTO-TO30 presents a TBE of 2.2 ± 0.6 nm, which is nearly 1 order of magnitude smaller than the other cases.

dx.doi.org/10.1021/am5072018 | ACS Appl. Mater. Interfaces 2015, 7, 765−773

This could be explained by the combination of the interdiffusion process of the Ti cations at the interface and the Sn/Cd stoichiometry gradient of the bulk CTO: both effects produce an interfacial layer (L_{1-2}), which might smoothly connect the conduction band offset between the surface L_0 layer and the bulk L_3 (Figure 9a), thereby favoring

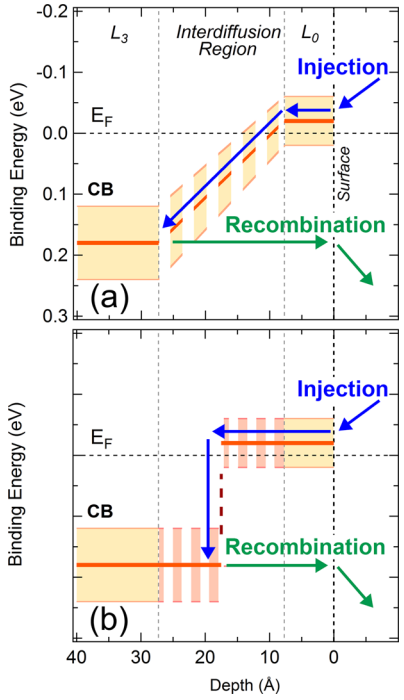

Figure 9. CB enlargements for the CTO-TO30: (a) interpretation of the interfacial layer (L_{1-2}) as a link between the band offset of L_0 and L_3 due to the cation interdiffusion process and (b) representation of the equivalent abrupt band offset.

the travel of the electrons with respect to the case of a potential barrier formed by a single sharp step (Figure 9b), which is distinctive of an abrupt TCO/BL heterojunction. In this way (Figure 9a), the electrons injected in the TiO_2 empty states should travel a shorter path at a constant flat band (L_0)—thereby decreasing the electron injection time—and then run down a smooth potential barrier (L_{1-2}), which acts as a buffer layer. In turn, the electrons in the CTO conduction band should pass through a larger potential barrier to undergo recombination. The combination of these effects is expected to yield the better performances observed for CTO-TO30 DSSC.

CONCLUSION

The present study was aimed to track possible Ti/Sn interdiffusion processes and Sn/Cd stoichiometry gradients at the nanostructured CTO-TO interface and, on this basis, extract a band alignment at the interface to be eventually related with the measured DSSC efficiency.

In the general frame of the studies on the physical and chemical properties at the origin of DSSC performances, the present work points out the relevance of considering cation substitution and interdiffusion at the interface, along with their effects on the VB and CB energy level profiles across the front contact that have been tracked by modeling of AR-XPS data.

In fact, by means of AR-XPS, we have evidenced a Sn/Cd stoichiometry gradient in the amorphous CTO film. Then, a cation interdiffusion between Ti and Sn has been evidenced at the heterointerfaces (CTO-TOs) between the CTO and different thin films of TiO_2 grown via RF-magnetron sputtering, as shown in the data analyzed on the basis of a four-effective layer model, which included two intermediate layers where Sn was replaced by Ti. In addition, we have evaluated the effective VB and CB band diagram for the CTO-TOs by using suitable energy gap values for CTO and TiO_2. Details of this band diagram qualitatively explain the observed efficiency variations on the basis of a reduced electron recombination along with an efficient charge injection across the junction.

AUTHOR INFORMATION

Corresponding Author

*Phone: ++39-030-2406716. E-mail: sangalet@dmf unicatt.it.

Author Contributions

The manuscript was written through contributions of all authors. All authors have given approval to the final version of the manuscript.

Notes

The authors declare no competing financial interest.

REFERENCES

(1) Johansson, E. M. J.; Lindblad, R.; Siegbahn, H.; Hagfeldt, A.; Rensmo, H. Atomic and Electronic Structures of Interfaces in Dye-Sensitized, Nanostructured Solar Cells. *ChemPhysChem* **2014**, *15*, 1006−1017.

(2) Mora-Seró, I.; Giménez, S.; Fabregat-Santiago, F.; Azaceta, E.; Tena-Zaera, R.; Bisquerta, J. Modeling and Characterization of Extremely Thin Absorber (ETA) Solar Cells Based on ZnO Nanowires. *Phys. Chem. Chem. Phys.* **2011**, *13*, 7162−7169.

(3) Hardin, B. E.; Snaith, H. J.; McGehee, M. D. The Renaissance of Dye-Sensitized Solar Cells. *Nat. Photonics* **2012**, *6*, 162−169.

(4) Jiang, D.; Hao, Y.; Shen, R.; Ghazarian, S.; Angela, R.; Zhou, F. Effective Blockage of the Interfacial Recombination Process at TiO_2 Nanowire Array Electrodes in Dye-Sensitized Solar Cells. *ACS Appl. Mater. Interfaces* **2013**, *5*, 11906−11912.

(5) Zheng, Y.; Klankowski, S.; Yang, Y.; Li, Y. Preparation and Characterization of TiO_2 Barrier Layers for Dye-Sensitized Solar Cells. *ACS Appl. Mater. Interfaces* **2014**, *6*, 10679−10686.

(6) Yang, Z.; Gao, S.; Li, T.; Liu, F. Q.; Ren, Y.; Xou, T. Enhanced Electron Extraction from Template-Free 3D Nanoparticulate Transparent Conducting Oxide (TCO) Electrodes for Dye-Sensitized Solar Cells. *ACS Appl. Mater. Interfaces* **2012**, *4*, 4419−4427.

(7) Braga, A.; Baratto, C.; Colombi, P.; Bontempi, E.; Salvinelli, G.; Drera, G.; Sangaletti, L. An Ultrathin TiO_2 Blocking Layer on Cd Stannate as Highly Efficient Front Contact for Dye-Sensitized Solar Cells. *Phys. Chem. Chem. Phys.* **2013**, *15*, 16812−16818.

(8) Bädeker, K. Uber die Elektrische Leitfähigkeit und die Thermoelektrische Kraft Einiger Schwermetallverbindungen. *Ann. Phys. (Leipzig, Ger.)* **1907**, *22*, 749−766.

(9) Gordon, R. G. Criteria for Choosing Transparent Conductors. *MRS Bull.* **2000**, *8*, 52−57.

(10) Wu, X.; Coutts, T. J.; Mulligan, W. P. Properties of Transparent Conducting Oxides Formed from CdO and ZnO Alloyed with SnO_2 and In_2O_3. *J. Vac. Sci. Technol. A* **1997**, *15*, 1057−1062.

(11) Nozik, A. J. Optical and Electrical Properties of Cd_2SnO_4: A Defect Semiconductor. *Phys. Rev. B* **1972**, *6*, 453−459.

(12) Hosono, H.; Yasukawa, M.; Kawazoe, K. Novel Oxide Amorphous Semiconductors: Transparent Conducting Amorphous Oxides. *J. Non-Cryst. Solids* **1996**, *203*, 334−344.

(13) Braga, A.; Baratto, C.; Bontempi, E.; Colombi, P.; Sberveglieri, G. Transparent Front Contact Optimization in Dye Sensitized Solar Cells: Use of Cadmium Stannate and Titanium Oxide by Sputtering. *Thin Solid Films* **2014**, *555*, 18−20.

(14) Kay, A.; Grätzel, M. Dye-Sensitized Core−Shell Nanocrystals: Improved Efficiency of Mesoporous Tin Oxide Electrodes Coated with

a Thin Layer of an Insulating Oxide. *Chem. Mater.* **2002**, *14*, 2930−2935.
(15) Kim, M. H.; Kwon, Y. U. Semiconducting Divalent Metal Oxides as Blocking Layer Material for SnO_2-Based Dye-Sensitized Solar Cells. *J. Phys. Chem. C* **2011**, *115*, 23120−23125.
(16) Hagfeldt, A.; Boschloo, G.; Sun, L.; Kloo, L.; Pettersson, H. Dye-Sensitized Solar Cells. *Chem. Rev. (Washington, DC, U.S.)* **2010**, *110*, 6595−6663.
(17) Yoo, B.; Kim, K.; Lee, D. K.; Ko, M. J.; Lee, H.; Kim, Y. H.; Kim, W. M.; Park, N. G. Enhanced Charge Collection Efficiency by Thin-TiO_2-Film Deposition on FTO-Coated ITO Conductive Oxide in Dye-Sensitized Solar Cells. *J. Mater. Chem.* **2010**, *20*, 4392−4398.
(18) Hart, J. N.; Menzies, D.; Cheng, Y. B.; Simon, G. P.; Spiccia, L. TiO_2 Sol−Gel Blocking Layers for Dye-Sensitized Solar Cells. *C. R. Chim.* **2006**, *9*, 622−626.
(19) Xia, J.; Masaki, N.; Jiang, K.; Wata, Y.; Yanagida, S. Importance of Blocking Layers at Conducting Glass/TiO_2 Interfaces in Dye-Sensitized Ionic-Liquid Solar Cells. *Chem. Lett.* **2006**, *35*, 252−253.
(20) Yu, H.; Zhang, S.; Zhao, H.; Will, G.; Liu, P. An Efficient and Low-Cost TiO_2 Compact Layer for Performance Improvement of Dye-Sensitized Solar Cells. *Electrochim. Acta* **2009**, *54*, 1319−1324.
(21) Kim, Y. J.; Lee, Y. H.; Lee, M. H.; Kim, H. J.; Pan, J. H.; Lim, G. I.; Choi, Y. S.; Kim, K.; Park, N. G.; Lee, C.; Lee, W. I. Formation of Efficient Dye-Sensitized Solar Cells by Introducing an Interfacial Layer of Long-Range Ordered Mesoporous TiO_2 Thin Film. *Langmuir* **2008**, *24*, 13225−13230.
(22) Que, L.; Lan, Z.; Wu, W.; Wu, J.; Lin, J.; Huang, M. Titanium dioxide quantum dots: Magic Materials for High Performance Underlayers Inserted into Dye-Sensitized Solar Cells. *J. Power Sources* **2014**, *268*, 670−676.
(23) Cameron, P. J.; Peter, L. M. Characterization of Titanium Dioxide Blocking Layers in Dye-Sensitized Nanocrystalline Solar Cells. *J. Phys. Chem. B* **2003**, *107*, 14394−14400.
(24) Lee, C. H.; Chiu, W. H.; Lee, K. M.; Hsiehb, W. F.; Wu, J. M. Improved Performance of Flexible Dye-Sensitized Solar Cells by Introducing an Interfacial Layer on Ti Substrates. *J. Mater. Chem.* **2011**, *21*, 5114−5119.
(25) Kraut, E. A.; Grant, R. W.; Waldrop, J. R.; Kowalczyk, S. P. Precise Determination of the Valence-Band Edge in X-Ray Photoemission Spectra: Application to Measurement of Semiconductor Inter face Potentials. *Phys. Rev. Lett.* **1980**, *44*, 1620−1623.
(26) Kraut, E. A.; Grant, R. W.; Waldrop, J. R.; Kowalczyk, S. P. Semiconductor Core-Level to Valence-Band Maximum Binding-Energy Differences. Precise Determination by X-ray Photoelectron Spectroscopy. *Phys. Rev. B* **1983**, *28*, 1965−1977.
(27) Drera, G.; Salvinelli, G.; Åhlund, J.; Karlsson, P.; Wannberg, B.; Magnano, E.; Sangaletti, L. Transmission Function Calibration of an Angular Resolved Analyzer for X-ray Photoemission Spectroscopy: Theory vs Experiment. *J. Electron Spectrosc. Relat. Phenom.* **2014**, *195*, 109−116.
(28) Yeh, J. J.; Lindau, I. Atomic Subshell Photoionization Cross Sections and Asymmetry Parameters: $1 \leq Z \leq 103$. *At. Data Nucl. Data Tables* **1985**, *32*, 1−155.
(29) Werner, W. S. M. Electron Transport in Solids for Quantitative Surface Analysis. *Surf. Interface Anal.* **2001**, *31*, 141−176.
(30) Tanuma, S.; Powell, C. J.; Penn, D. R. Calculation of Electron Inelastic Mean Free Paths (IMFPs) VII. Reliability of the TPP-2M IMFP Predictive Equation. *Surf. Interface Anal.* **2003**, *35*, 268−275.
(31) Tilinin, I. S.; Jablonski, A.; Zemek, J.; Hucek, S. Escape Probability of Signal Photoelectrons From Noncrystalline Solids: Influence of Anisotropy of Photoemission. *J. Electron Spectrosc. Relat. Phenom.* **1997**, *97*, 127−140.
(32) Jablonski, A. Transport Cross Section for Electrons at Energies of Surface-Sensitive Spectroscopies. *Phys. Rev. B* **1998**, *58*, 16470−16480.
(33) Tougaard, S. Universality Classes of Inelastic Electron Scattering Cross-Sections. *Surf. Interface Anal.* **1997**, *25*, 137−154.
(34) Goldfarb, I.; Ohlberg, D. A. A.; Strachan, J. P.; Pickett, M. D.; Yang, J. J.; Medeiros-Ribeiro, G.; Williams, R. S. Band Offsets in Transition-Metal Oxide Heterostructures. *J. Phys. D: Appl. Phys.* **2013**, *46*, 295303−295309.
(35) Bird, R. J.; Swift, P. Energy Calibration in Electron Spectroscopy and the Redetermination of Some Reference Electron Binding Energies. *J. Electron Spectrosc. Relat. Phenom.* **1980**, *21*, 227−240.
(36) NIST X-ray Photoelectron Spectroscopy Database, http://srdata.nist.gov/xps/.
(37) Chambers, S. A.; Droubay, T.; Kaspar, T. C.; Gutowski, M. Experimental Determination of Valence Band Maxima for $SrTiO_3$, TiO_2, and SrO and the Associated Valence Band Offsets with Si (001). *J. Vac. Sci. Technol. B* **2004**, *22*, 2205−2215.
(38) Raviendra, D.; Sharma, J. K. Electroless Deposition of Cadmium Stannate, Zinc Oxide, and Aluminum Doped Zinc Oxide Films. *J. Appl. Phys.* **1985**, *58*, 838−844.
(39) Baratto, C.; Ponzoni, A.; Ferroni, M.; Borgese, L.; Bontempi, E.; Sberveglieri, G. Sputtering Deposition of Amorphous Cadmium Stannate as Transparent Conducting Oxide. *Thin Solid Films* **2012**, *520*, 2739−2744.
(40) Dou, Y.; Egdell, R. G. Surface Properties of Indium-Doped Cd_2SnO_4 Ceramics Studied by EELS and Photoemission Spectroscopy. *Surf. Sci.* **1997**, *372*, 289−299.
(41) Meng, T.; McCandless, B.; Buchanan, W.; Kimberly, E.; Birkmire, R. Cadmium Tin Oxide Thin Films Deposited by RF Magnetron Sputtering for Photovoltaic Applications. *J. Alloys Compd.* **2013**, *556*, 39−44.
(42) Scanlon, D. O.; Dunnill, C. W.; Buckeridge, J.; Shevlin, S. A.; Logsdail, A. J.; Woodley, S. M.; Richard, C.; Catlow, A.; Powell, M. J.; Palgrave, R. G.; Parkin, I. P.; Watson, G. W.; Keal, T. W.; Sherwood, P.; Walsh, A.; Sokol, A. A. Band Alignment of Rutile and Anatase TiO_2. *Nat. Mater.* **2013**, *12*, 798−801.
(43) Jang, K.; Hong, E.; Kim, J. H. Effect of an Electrodeposited TiO_2 Blocking Layer on Efficiency Improvement of Dye-Sensitized Solar Cell. *Korean J. Chem. Eng.* **2012**, *29*, 356−361.
(44) Waita, S. M.; Aduda, B. O.; Mwabora, J. M.; Niklasson, G. A.; Granqvist, C. G.; Boschloo, G. Electrochemical Characterization of TiO_2 Blocking Layers Prepared by Reactive DC Magnetron Sputtering. *J. Electroanal. Chem.* **2009**, *637*, 79−83.
(45) Meng, L.; Li, C. Blocking Layer Effect on Dye-Sensitized Solar Cells Assembled with TiO_2 Nanorods Prepared by DC Reactive Magnetron Sputtering. *Nanosci. Nanotechnol. Lett.* **2011**, *3*, 181−185.
(46) Hore, S.; Kern, R. Implication of Device Functioning due to Back Reaction of Electrons via the Conducting Glass Substrate in Dye Sensitized Solar Cells. *Appl. Phys. Lett.* **2005**, *87*, 263504−263507.
(47) Peng, B.; Jungmann, G.; Jäger, C.; Haarer, D.; Schmidt, H. W.; Thelakkat, M. Systematic Investigation of the Role of Compact TiO_2 Layer in Solid State Dye-Sensitized TiO_2 Solar Cells. *Coord. Chem. Rev.* **2004**, *248*, 1479−1489.
(48) Law, M.; Greene, L. E.; Radenovic, A.; Kuykendall, T.; Liphardt, J.; Yang, P. ZnO−Al_2O_3 and ZnO−TiO_2 Core−Shell Nanowire Dye-Sensitized Solar Cells. *J. Phys. Chem. B* **2006**, *110*, 22652−22663.